Effect of Microstructure on Hydrogen-Induced Cracking in Sour Service Pipeline Steel

M. O'Brien[1], J.G. Speer[1], K. O. Findley[1]

[1]Colorado School of Mines
1400 Illinois St, Golden, CO 80401
Phone: 208-604-3843
Email: marobrie@mines.edu

Keywords: Hydrogen-induced cracking, pipeline steel, grain boundary misorientation

INTRODUCTION

Steels used for sour service applications in the oil and gas industry are subjected to corrosive internal environments containing high partial pressures of hydrogen sulfide (H_2S). During sour service, the presence of H_2S promotes enhanced hydrogen ingress into the steel and subsequent internal cracking, a process called hydrogen-induced cracking (HIC). The diffusion of hydrogen atoms and subsequent cracking is affected by the microstructural features present in the steel in two ways: local diffusivity and hydrogen "trapping". The steels utilized for these applications are fine grained thermomechanically processed (TMP) alloys with complex microstructures that can include microconstituents such as polygonal ferrite, quasi-polygonal ferrite, pearlite, martensite/austenite (M/A) microconstituents, non-metallic inclusions, and carbonitride precipitates.

Elongated MnS inclusions and hard bands due to segregation are deleterious to HIC resistance[1-3], so steel cleanliness and inclusion shape control measures have been utilized to mitigate these factors[4]. Higher strength grades are also more susceptible to HIC. NACE MR0175/ISO 15156 suggests a maximum yield strength of 116 ksi for steels used in sour service applications.[5] In practice however, steels with much lower yield strength, such as 60 ksi, are used to avoid HIC.

HIC can interact with multiple microstructural features besides inclusions in steel alloys. In higher strength grades that contain M/A microconstituents, there is some speculation through qualitative fracture surface analysis that M/A regions are preferential HIC initiation and propagation sites.[3, 6-9] However, no studies have determined quantitatively whether M/A constituents occur with greater frequency directly adjacent to cracks than in the microstructure. Further investigation is necessary to evaluate the influence of M/A microconstituents on HIC propagation. HIC results in both transgranular and intergranular cracking through the ferritic microstructure.[10-15] In TMP line pipe steels, texture can result from processing,[16] which can affect HIC propagation. For example, it has been hypothesized that the presence of grains with {001} planes parallel to the rolling plane have increased HIC susceptibility.[10,11,17]

The current work characterizes the microstructure of an X70 steel before and after hydrogen charging. The frequency of occurrence of M/A microconstituents both in the as-received and cracked X70 steel is compared to determine if M/A constituents crack more frequently than other microstructural constituents. Electron backscatter diffraction (EBSD) is used to assess the effect of local crystallographic orientation on HIC in relation to the AR microstructure. EBSD is also used to evaluate the nature of transgranular crack propagation.

EXPERIMENTAL PROCEDURE

Table I shows the chemical composition of the API X70 steel used in this study to investigate the effect of higher strength TMP microstructures on HIC resistance. Samples of the X70 steel were charged with hydrogen using either NACE Standard TM-0284[18] or a cathodic charging method.[19] The samples were sectioned in the ND-RD plane, mounted in Bakelite®, ground, and polished to 1 μm grit using standard metallographic procedures; then, the specimens were vibro-polished using 0.02 μm colloidal silica suspension for several hours. Electron backscatter diffraction (EBSD) patterns were obtained using both a JEOL-7000 field emission scanning electron microscope (FE-SEM) and a FEI Helios Nanolab 600i FE-SEM. All EBSD scans were obtained using an accelerating voltage of 20 kV and a 0.05 μm step size. The EBSD data were obtained at a 50 nm step size.

Table I – Chemical Composition of As-Received X70 Plate Steel in wt.% [16]

wt.%	C	Mn	Si	Ni	Cr	Ti	Mo	Nb
X70	0.050	1.59	0.3	0.01	0.26	0.013	0.09	0.066

V	Al	N	S	P	Cu
0.005	0.026	0.0081	0.003	0.010	0.01

Cracks were identified using a secondary electron (SE) detector and EBSD scans were then taken. Cracks were identified in the EBSD scans as wide regions with confidence index (CI) values less than 0.2. In order to assess boundary cracking susceptibility, misorientation matrices were calculated across cracks using a semi-automated method. A pair of orientations across a crack path was selected manually; then, the misorientation matrix was calculated automatically by the OIM^{TM} Analysis software. The selected orientations were taken approximately perpendicular to the crack direction less than 1 μm from the crack edge, and 0.2 to 0.4 μm apart in the rolling direction.

EBSD was also employed to evaluate interaction of HIC with M/A microconstituents, which were identified as distinct regions of low image quality around 1-2 μm wide in the rolling direction that were not associated with surface contamination. If a region of M/A intersected the crack in the image quality map, the length of the intersection was measured. The ratio of the cracked M/A length to the total crack length was measured. Over 1,000 μm in crack length was measured for this study.

Secondary electron (SE) micrographs were used to assess the line fraction of M/A constituents in the as-received (AR) microstructure for comparison to the line fraction of M/A along cracks. A byproduct of the vibropolishing sample preparation step is a light etch of the carbon rich regions. This light etch, combined with a relatively short working distance of ~9.5 mm, was used in combination with a SE detector in the JEOL 7000 FESEM to image the M/A microconstituents. This polishing procedure was chosen over conventional etching with 2 pct nital, because the 2 pct nital etch results in topographic contrast that can overpower the subtle contrast necessary to resolve the M/A microconstituents. Because a majority of the cracking observed in X70 occurred at the centerline, the line fraction of M/A constituents was also inspected within a region 5 μm above and below the centerline in the as-received X70. Line lengths that intersected regions identified as M/A were measured, and the total M/A length over the total line length was calculated. Twenty micrographs were obtained from the centerline region, resulting in approximately 1,900 μm of total line length assessed.

RESULTS AND DISCUSSION

The following section presents an overview of the as-received X70 microstructure followed by results and analysis of HIC interaction with M/A microconstituents, grain boundaries, and transgranular fracture planes in the X70 steel.

As-Received Microstructure

The X70 microstructure contains non-equiaxed highly substructured ferritic constituents with M/A microconstituents. EBSD micrographs were used to examine grain orientation, substructure, and morphology in the AR X70 microstructure. Figure 1a is an image quality (IQ) map with boundary misorientations overlaid, and Figure 1b is an inverse pole figure (IPF) map with points having less than 0.2 confidence index (CI) shown in black to allow for ease of identification of grain boundaries. Figure 1a and b indicate that the X70 steel contains both small eqiuaxed grains around 1 or 2 μm in diameter and larger (8 to 10 μm in diameter) elongated grains with several low angle boundaries having 2 to 15° misorientation as shown in Figure 1a. An important feature of note in the X70 microstructure is highlighted by dashed lines in Figure 1a and b which is a large region composed of grains with similar orientations. The boundary misorientations from 2 to 15° within these regions could be of importance during cracking, as dislocations and boundary structures play a role in hydrogen trapping or provide a path for crack propagation. These types of grains grouped with similar orientations are not as prevalent in lower strength alloys. The boundary misorientations from 2 to 15° within these large grains could be of importance during cracking, as dislocations and boundary structures can trap hydrogen or provide a path for crack propagation. The measured grain diameters ranges from 1 to 5 μm with a smaller number of large grains from 7 to 9 μm.

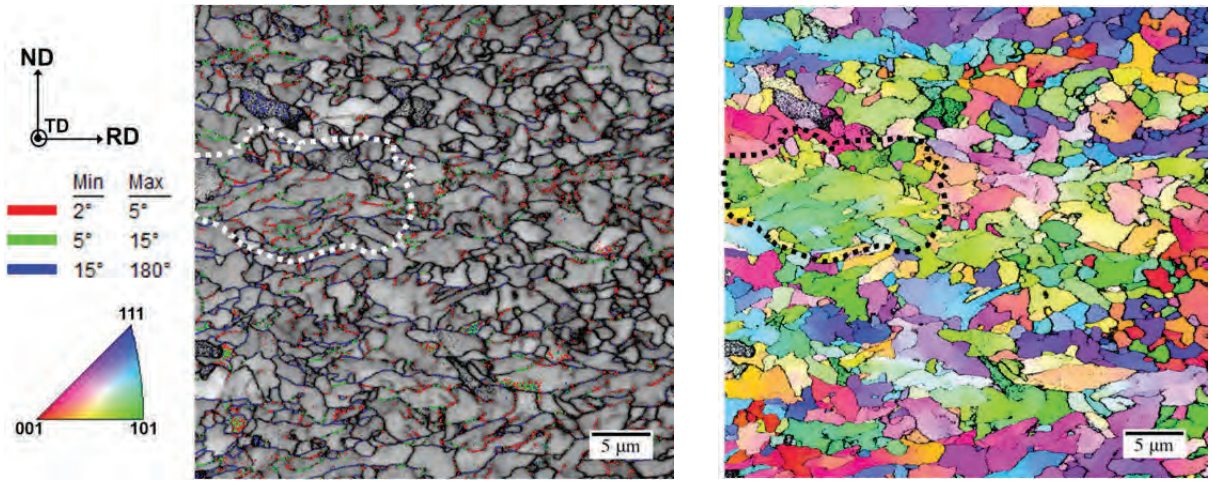

(a) (b)

Figure 1. EBSD micrographs from the AR X70 steels where (a) is an IQ map with points having less than 0.2 CI displayed in black and grain boundary coloring overlaid according to the legend to the left and (b) is an IPF map of same region, with the stereographic triangle shown on the left, and points less than 0.2 CI displayed in black *(color image – see electronic copy)*.

HIC Interaction with M/A

Figure 2 is a photograph of a sample of the X70 alloy that was hydrogen charged using the procedure outlined in NACE Standard TM-0284. The crack in Figure 2 is about 10 mm in length in the rolling direction at the centerline. Most of the cracks in X70 samples occurred along the centerline but varied in length. Figure 3a is a SE micrograph from a vibropolished AR X70. An example of an M/A microconstituent is shown in the higher magnification image from the same region. Similarly, Figure 3b is an example EBSD image quality map showing M/A regions next to HIC. The ratio of M/A to total line length in the AR microstructure and the ratio of M/A. length to total crack length in hydrogen charged samples are tabulated in Table II. The line fraction of M/A microconstituents along a crack is approximately 4 pct., while the line fraction of M/A constituents at the centerline of the as-received microstructure is 3.6 pct. This small difference between M/A line fraction along the crack path compared to the line fraction of M/A in the AR microstructure indicates that M/A microconstituents do not preferentially crack relative to the ferritic microstructure, in contrast to previous literature. It is important to note, however, that this line fraction assessment does not directly quantify the role that M/A constituents have in hydrogen trapping and diffusion, but rather assesses the vulnerability of M/A to cracking compared to the ferritic matrix.

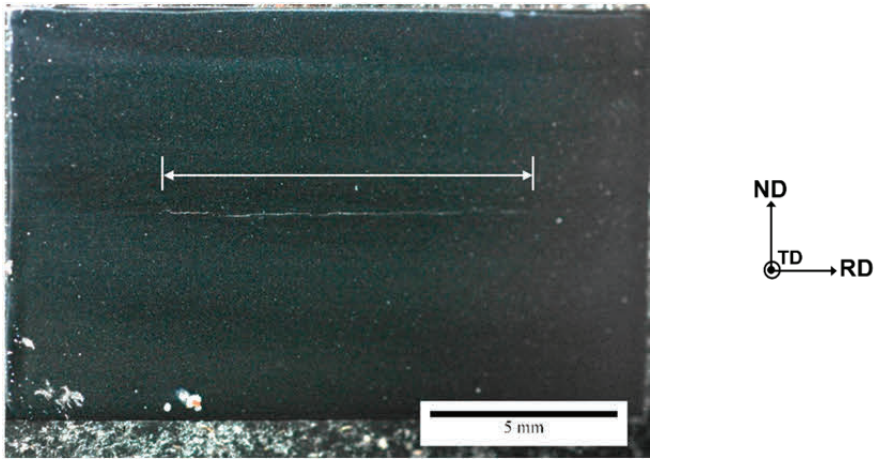

Figure 2. Photograph of a crack found at the centerline of the X70 sample charged with the NACE TM0284 charging method.[18]

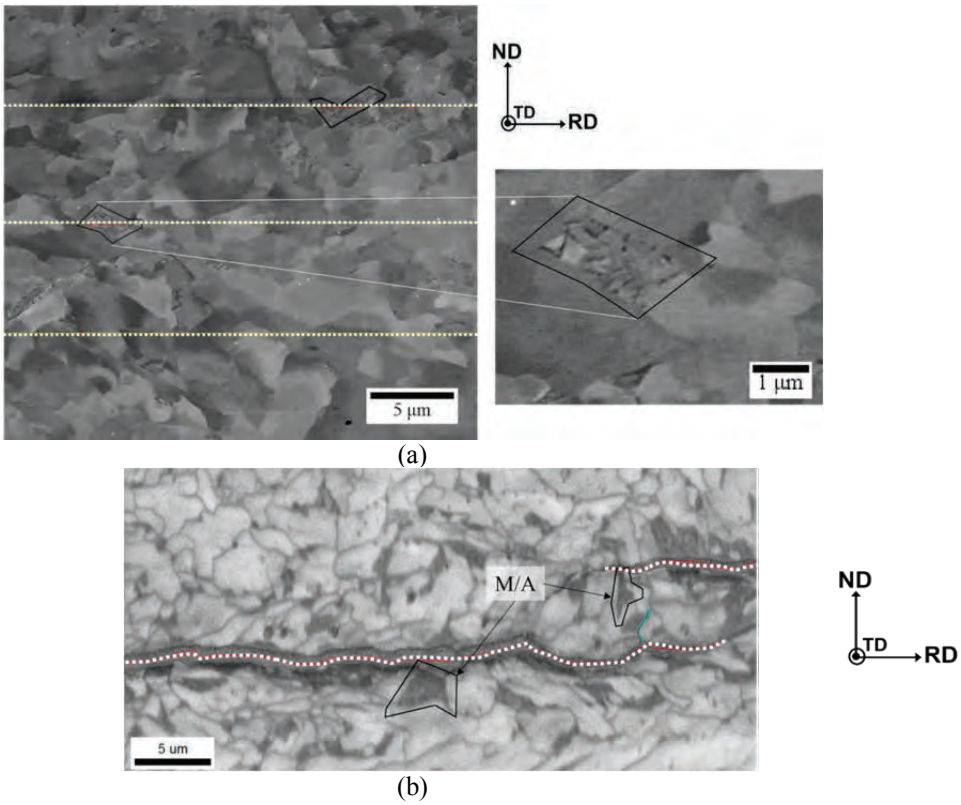

Figure 3. Micrographs from the X70 steel where (a) is a SE micrograph from the AR X70 steel with some of the M/A constituents identified, and dashed white lines represent the measurement lines. (b) EBSD IQ map obtained from an X70 steel charged with hydrogen using NACE TM-0284[18] with M/A microconstituents directly adjacent to cracks identified as distinct dark regions and outlined in black. In addition, the white dashed lines are examples of crack length measurements taken using ImageJ software.

Table II – Crack lengths and ratios of M/A cracking to total crack length

	Total Length (µm)	M/A Length (µm)	Ratio of M/A to Total Length
NACE	1020	42	0.0407
As-received	1911	69	0.0359

HIC Interaction with Boundaries

Boundaries are defined using five parameters; three describe the misorientation matrix necessary to bring two neighboring grain orientations into coincidence,[20,21] and two describe the boundary plane orientation.[22] The misorientation matrix describes the axis and angle of rotation necessary to bring two orientations into coincidence. Examinations of boundary character often consider misorientation angle as a function of frequency of occurrence, known as Mackenzie plots.[20] Mackenzie plots from the AR microstructure and grains adjacent to cracked boundaries in the hydrogen charged samples are shown in Figure 4, where the data represent boundaries that fall within a 5° bin. The misorientation angle profiles for the cracked boundaries from the cathodically charged and the NACE TM0284 charged X70 alloy are similar. Both charging conditions had the highest number fraction of cracked boundaries at 5 to 10° misorientation and another peak around 50-55° misorientation. Because the two charging conditions trend so similarly, the average number fraction was calculated and is represented as a dotted line in Figure 4. Very low angle boundaries between 2 to 5° misorientation appear at a much lower number fraction in the cracked boundaries than in the AR X70 material. In addition, boundaries with about 5 to 20° misorientation appear more frequently in the cracked boundaries than in the AR material. The misorientation distributions for both the AR and cracked boundaries nearly coincide from 25 to 45° misorientation. Lastly, the cracked boundaries have a lower number fraction in the 45 to 62.5° misorientation range than the AR X70 specimens. This analysis of the misorientation angle distributions could indicate that 5 to 20° misorientations are more susceptible to cracking, while 2 to 5° and 45 to 60° misorientations are less susceptible.

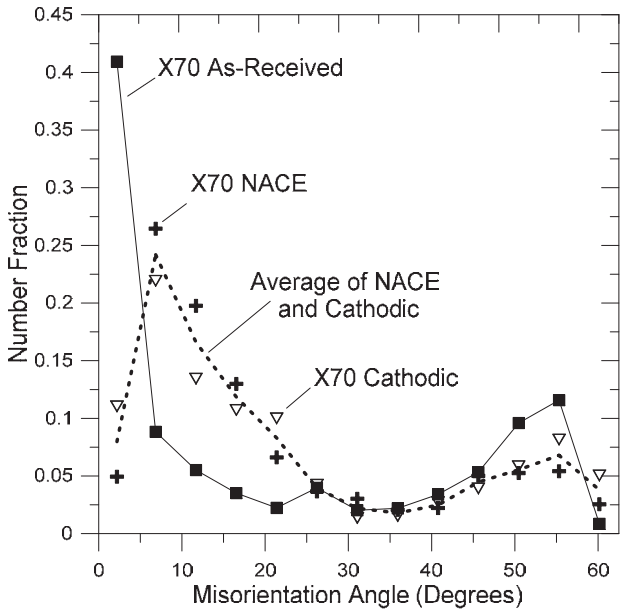

Figure 4. Mackenzie plot of number fraction of misorientation angles for the X70 AR microstructure and cracked boundaries averaged for the NACE and cathodically charged X70 specimens plotted with a dashed line.

To gain a more complete understanding of the boundary structures present in a material, both the misorientation angle and axis of rotation in the misorientation matrix must be considered. The misorientation matrix is most often described using an angle/axis pair, where the misorientation angle (θ) is the minimum rotation necessary to bring two adjacent grains into coincidence, and the misorientation axis ([*uvw*]) is the direction about which the rotation occurs.[23] Misorientation angle and axis pairs are often denoted using the notation θ || [*uvw*], meaning a misorientation of θ° about a [*uvw*] axis. This notation will also be used in the current work. Misorientation distribution functions (MDF) are calculated from EBSD data and used to represent boundary character.[20-25] MDFs in Rodriguez-Frank (RF) space use the misorientation axis and angle to calculate the Rodriguez vector $\overline{\boldsymbol{R}}$, which is shown in Figure 5 where *uvw* is the unit vector axis of misorientation and θ is the angle of misorientation.[26] The components of $\overline{\boldsymbol{R}}$ are $(\mathbf{r_1}, \mathbf{r_2}, \mathbf{r_3})$, and their unit vectors are shown in Figure 5. The shape of RF space is highly dependent on crystal symmetry. Due to the symmetry implicit in cubic structures, the fundamental zone of RF space, represented as a truncated cube, can be reduced to the shape shown in Figure 5 for materials with cubic symmetry.

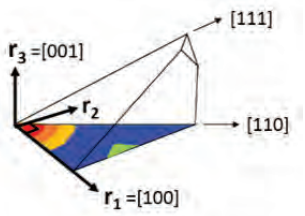

$$\overline{\boldsymbol{R}} = \overline{uvw}\tan(\theta/2)$$

Figure 5. Schematic of Rodrigues-Frank space for cubic structures used for misorientation distribution functions.

Figure 6 is an MDF plot in RF space of the AR X70 microstructure (contour plot) with black dots overlaid that signify discrete points calculated across cracked boundaries in both NACE and cathodically charged conditions. The legend in Figure 6 is in units of multiples of a random distribution (MRD). The red regions in Figure 6 indicate maxima that occur in the X70 MDF with MRD of about 24 and near a 43.6° || <100> axis/angle pair. The next highest value in MRD appears around 8.3 in a region near 31.6° || <110>. Lastly, there is a region with 4.9 MRD that is near 60° || <111> in axis/angle notation. Using the OIM™ software, the number fraction of each of these boundary types in the as-received X70 microstructure was calculated for data points with CI greater than 0.2. The resulting number fractions were 0.059 at 60° || <111>, 0.0029 at 43.6° || <100>, and 0.00049 at 31.6° || <110>, all in terms of number fraction.

A comparison of the AR microstructure to the hydrogen charged microstructure in RF space (Figure 6) reveals that the misorientations across cracks (black dots) are randomly distributed through RF space with a few exceptions. A large frequency of low angle boundary cracks in the hydrogen charged samples are shown by the high density of black dots representing cracked misorientations, which is consistent with the large number fraction of 5 to 10° misorientation in Figure 4. Interestingly, Figure 6 also reveals that there is a lack of black dots near the 43.6° || <100> misorientation, which

could indicate that misorientations near 43.6° || <100> are resistant to HIC. It is important to note that Figure 6 does not distinguish between ferrite grain boundaries and phase boundaries. The resistance of 43.6° || <100> boundaries to crack has also been observed by other researchers in low carbon ferrite/pearlite steel.[11] Similarly, there are not many black dots near the 31.6° || <110> misorientations. Therefore, boundaries with misorientation near 31.6° ||<110> could also be resistant to cracking but are present in the AR microstructure much less frequently than the 43.6° ||<100> boundaries. In contrast, the 60° || <111> misorientations do not appear resistant to cracking.

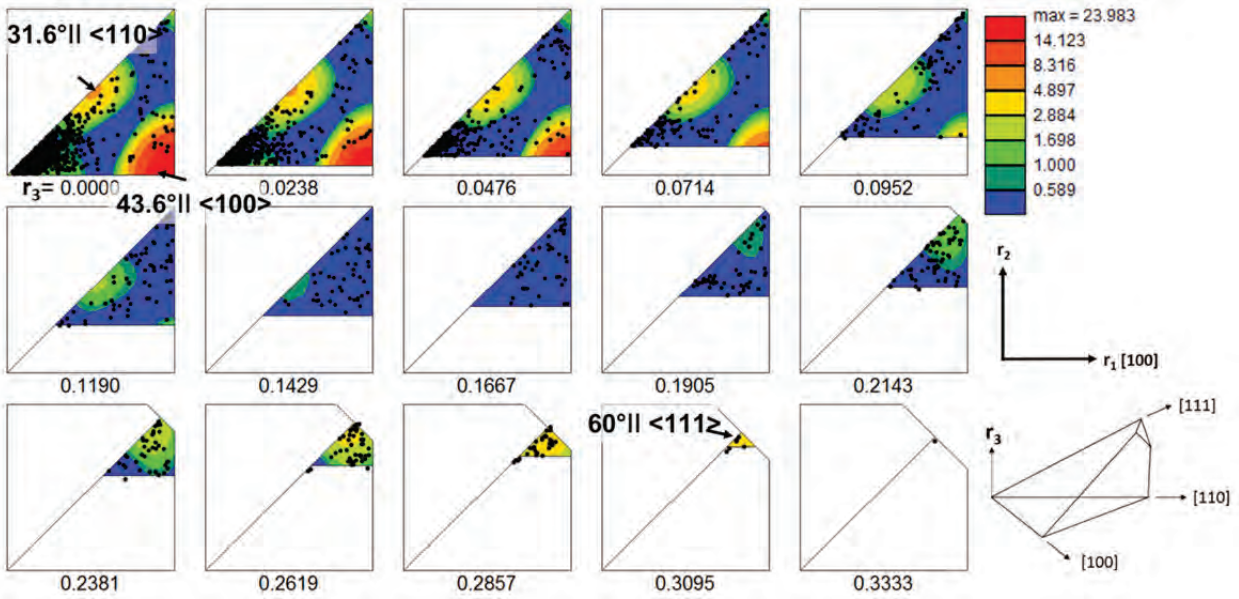

Figure 6 Misorientation distribution function in RF space for the as-received X70 steel with discrete misorientation angle/axis pairs from cracked boundaries overlaid as black dots. Locations of three special boundaries with high multiples of a random distribution are also overlaid for reference *(color image – see electronic copy)*.

Figures 7a, b and c are IQ maps from the AR X70 steel with misorientation (Figure 7a), phase (Figure 7b), and 43.6° ||<100> ± 5° misorientation (Figure 7c) overlaid; with all data points included. Figure 7a shows there is substructure within some ferrite grains as indicated by the red 2 to 5° misorientation boundaries; boundaries with these misorientations had relatively high number fractions in the Mackenzie plot shown in Figure 5. There is a small peak in the Mackenzie plot for the as-received microstructure near 30° misorientation as shown in Figure 5; these boundaries are included in the 25-45° misorientations, shown as light blue points in Figure 7a. Figure 7b is a phase map with ferritic regions colored in red and cementite regions colored in green. The regions that appear to be rich in cementite in Figure 7b largely correlate to the regions with 25 to 45° misorientation in Figure 7a, including boundaries near 30° misorientation. In addition, the regions rich in cementite are low in confidence index.

The location of misorientations within ± 5° of 43.6° || <100> are shown on the IQ map in Figure 7c. Regions dense in 43.6° ||<100> boundaries are correlated to low confidence indices in the as-received microstructure, Further, the regions rich in 43.6° ||<100> misorientations in Figure 7c largely correspond to regions containing cementite in Figure 7b. The 43.6° || <100> misorientations all appear within ferrite grains rather than between grains, which indicates that the features are not grain boundaries, but rather are likely to represent phase boundaries between ferrite and cementite. It is important to note that the RF space used in the previous figures is for cubic symmetry, while Fe_3C has an orthorhombic lattice that is represented by a different fundamental zone shape in RF space. Thus, the specific axis/angle misorientation pairs associated with the cementite regions may not be those shown in the cubic RF space. However, the cubic RF space provides a tool to indicate regions in the microstructure dense in boundaries of a specific misorientation. Further work is necessary to determine the actual misorientations between ferrite and cementite constituents, which are currently highlighted as boundaries near 43.6° ||<100>.

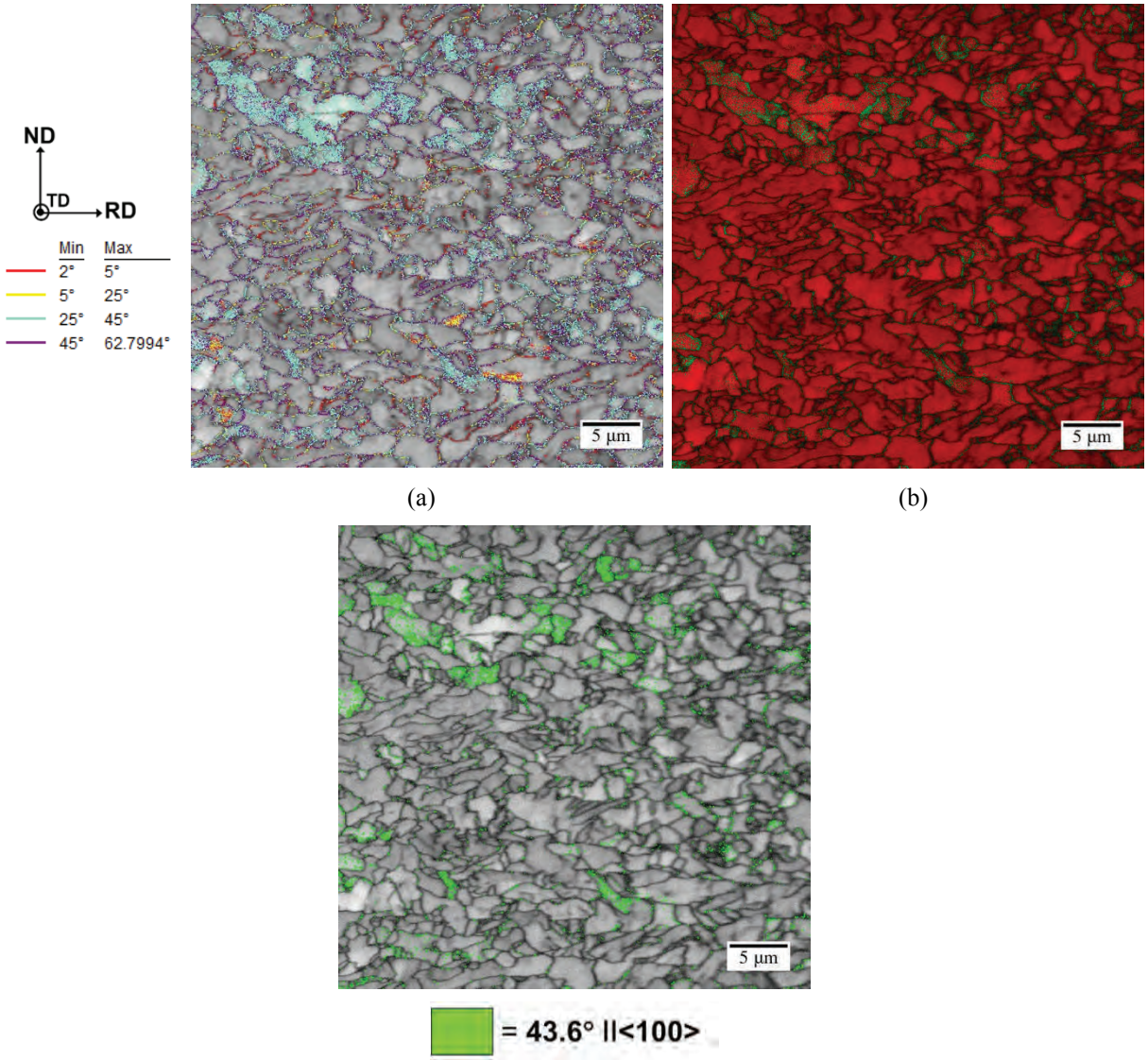

(a) (b)

(c)

Figure 7. EBSD IQ maps from the AR X70 steel (a) with boundary misorientations overlaid per the legend to the left, (b) with phases overlaid where red indicates a point indexed as ferrite and green indicates a point indexed as cementite, and (c) with special 43.6° ||<100> boundaries overlaid in green *(color image – see electronic copy).*

An example of a cracked region is shown in Figure 8a and b, which are micrographs of a cracked region from an X70 sample cathodically charged with hydrogen. Figure 8a is an EBSD IQ map with boundary misorientations adjacent to the crack overlaid and M/A regions identified. Figure 8b is an IPF map with data for with CI is less than 0.2 shown in black and average misorientations across the crack overlaid. Figure 8b contains a large region with a similar orientation. These large regions of similar orientation are often observed adjacent to cracks. There is both dislocation substructure and high angle grain boundaries present within this region shown in Figure 8a. It is interpreted that the cracks through the low misorientation regions (2 to 5°) are transgranular, and thus, the crack propagated both transgranularly and intergranularly in this region. The range of misorientations overlaid in Figure 8b is reflective of that shown in the Mackenzie plot, where the majority of the cracking occurs in misorientations with 5 to 25°, with a smaller amount of cracking from 45 to 60° misorientation. It is possible that the high density of boundaries less than 25° misorientation within these large regions in the X70 steel are more susceptible to cracking, as 5 to 25 ° misorientation boundaries were shown to be more susceptible to HIC (Figure 4).

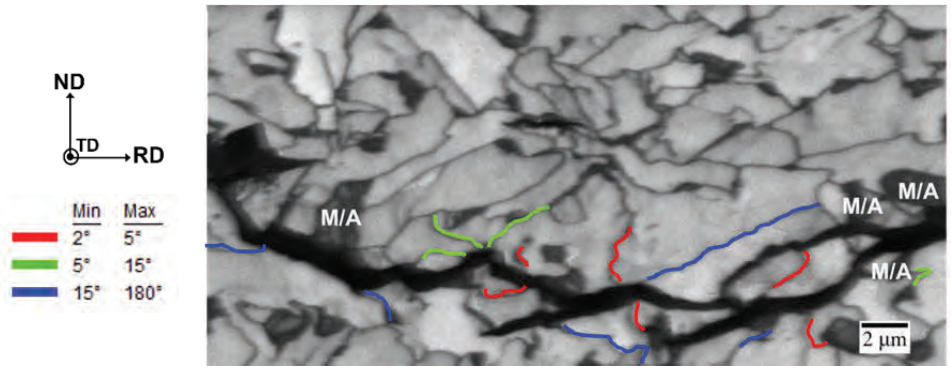

(a)

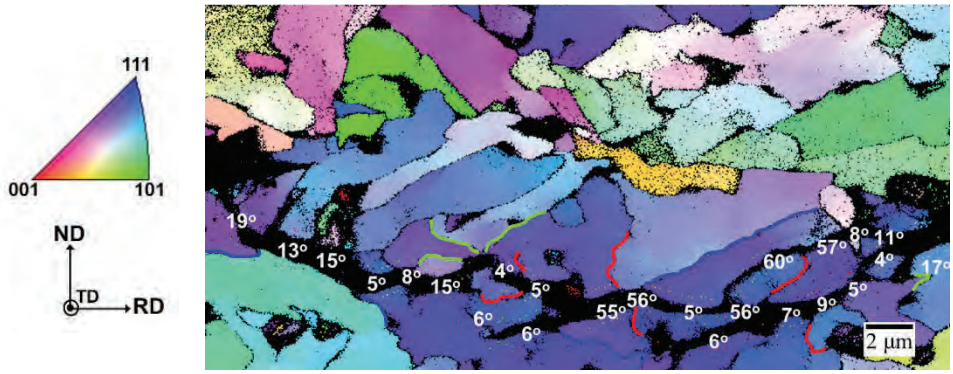

(b)

Figure 8. Micrographs obtained from an X70 steel charged using the cathodic charging method where (a) is an EBSD IQ map with grain boundary misorientations adjacent to the crack overlaid per the legend to the left, and (b) is an EBSD IPF map with points having less than 0.2 CI shown in black and average misorientations across the crack displayed *(color image – see electronic copy)*.

Figure 9 is a confidence index map with 43.6° || <100> ± 2.8° misorientations overlaid in green and the crack overlaid in red. The discrete misorientations calculated across the crack suggest that boundaries near 43.6° || <100> axis/angle pairs were resistant to cracking as discussed earlier (Figure 6). An example of a region in which the crack appears to avoid grains dense in boundaries near 43.6° || <100> is shown in Figure 9. The crack propagated adjacent to grains dense in boundaries near 43.6° || <100>, but the crack did not propagate through any of these regions. One example non-cracked region is highlighted with a white arrow in Figure 9. The HIC resistance of these regions, which also correspond to regions with greater amounts of cementite in EBSD maps, could be due to hydrogen trapping of the carbides and subsequent lack of hydrogen available for cracking.

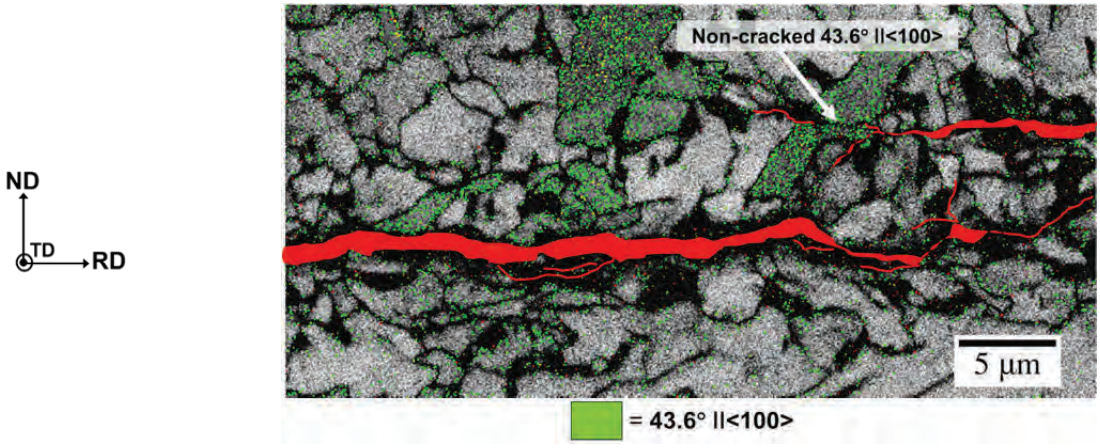

Figure 9. EBSD confidence index map from an X70 sample charged using the NACE TM0284 method with boundaries near 43.6° || <100> overlaid in green and the crack overlaid in red *(color image – see electronic copy)*.

Transgranular HIC Analysis

The crystallographic plane on which cracks occur is of interest to determine the mechanism by which cracks propagate transgranularly. In materials not exposed to hydrogen, brittle transgranular fracture occurs along {100} cleavage planes. The presence of hydrogen can allow for hydrogen enhanced localized plasticity (HELP) and adsorption induced dislocation emission (AIDE), which in turn can promote slip based transgranular fracture.[27] In Figure 10, an IPF map from a cathodically charged X70 specimen with CI less than 0.2 shown in black, shows various regions of transgranular cracking highlighted and labeled as A, B, C, and D. The crack trace is compared to traces of the nearest cleavage and slip planes in Figure 11. Region A is analyzed in Figure 11a, where all the crystallographically equivalent cleavage plane traces are shown on the left, and the equivalent {110} type slip plane traces are shown in the middle. The figure on the right in Figure 11a is a pole figure in the sample reference frame with the crack trace shown as a solid line. The closest slip and cleavage plane traces to the crack plane trace were obtained from the data produced by the OIM software and plotted on the stereographic projection to the right in Figure 11a. The crack trace in Region A, shown in Figure 11a, is closest to a slip plane. The cracks in Region B and Region C, shown in Figure 11b and Figure 11c, respectively, are also closer to slip plane traces than cleavage plane traces. The exception lies in Region D, shown in Figure 11d, where the crack trace is closest to a cleavage plane trace. Overall, the X70 alloy exhibited transgranular cracking near both slip and cleavage plane traces. Regions where the crack trace was closest to {110} slip plane traces, such as Regions A, B and C, could indicate that hydrogen is indeed playing a role in enhancing slip and affecting the plane of transgranular cracking.

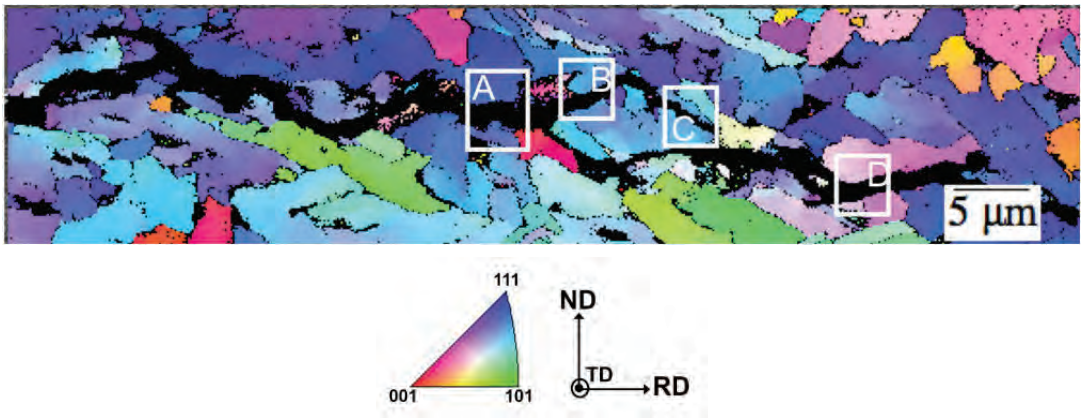

Figure 10. EBSD IPF map with CI <0.2 shown in black and regions for transgranular cracking analysis (A, B, C, and D) highlighted *(color image – see electronic copy)*.

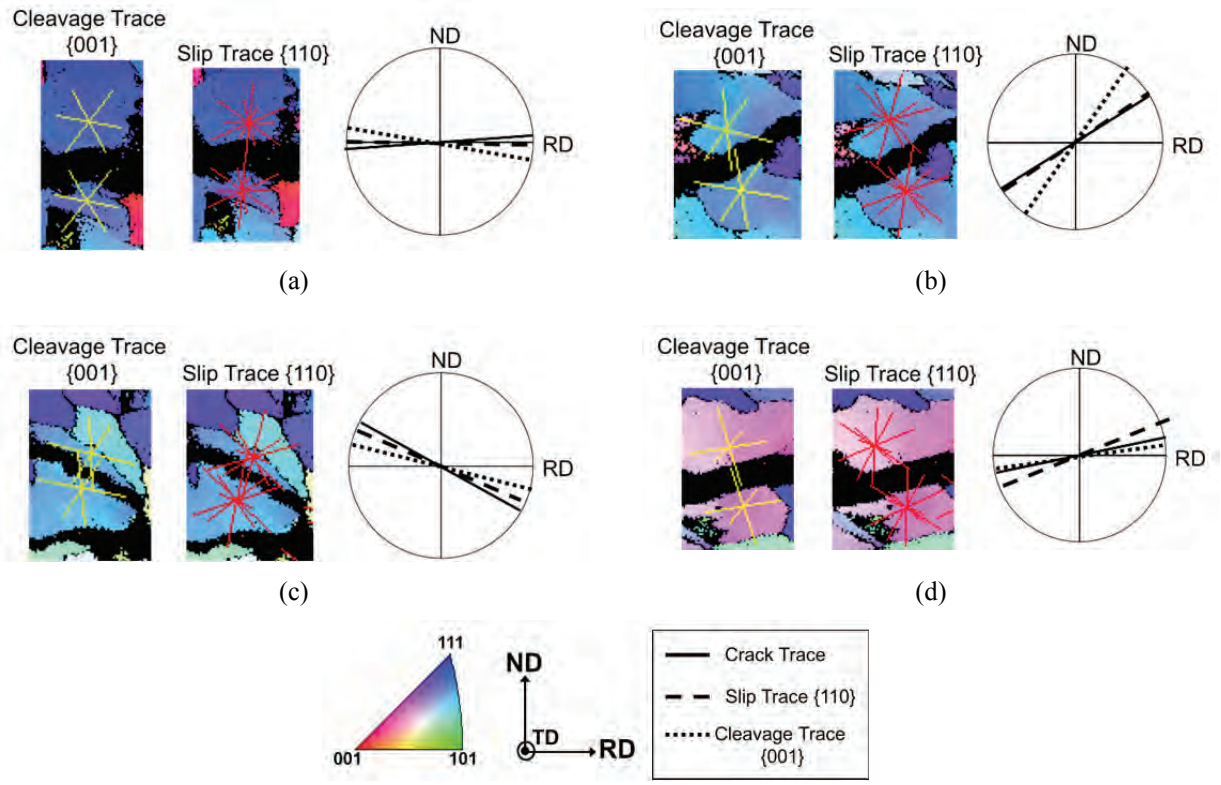

Figure 11. IPF maps with {001} cleavage traces (left) and {110} slip traces (right) overlaid, with a pole figure in the sample reference frame with the crack trace and closest slip and cleavage traces overlaid per the legend at bottom. Figures 11a, b, c, and d correlate to regions A, B, C and D shown in Figure 10, respectively *(color image – see electronic copy).*

CONCLUSIONS

Microstructural and crystallographic aspects of hydrogen-induced cracking were examined in X70 line pipe steel, with attention to the behavior of M/A microconstituents and phase and grain boundaries. The ratio of M/A microconstituents in the rolling direction along the centerline in the AR X70 material was compared to the ratio of M/A microconstituents adjacent to cracks. The ratios of M/A to total line length in the AR microstructure and along cracks in hydrogen charged samples were both approximately 4 pct, indicating that M/A microconstituents are not found more frequently along cracks than in the AR microstructure. This observation in turn indicates that HIC does not preferentially seek out M/A microconstituents.

Very low angle boundaries from 2 to 5° misorientation occurred frequently in the AR X70 microstructure and were found with less frequency in cracked regions. However, boundaries with 5 to 25° misorientation cracked more often than their frequency in the AR microstructure. Therefore, the large substructured grains rich in 5 to 25° misorientation boundaries might be more vulnerable to HIC. The presence of grains rich in cementite were resistant to cracking. The HIC resistance of these regions could be due to a local decrease in diffusible hydrogen due to hydrogen trapping at cementite precipitate interfaces.

Lastly, an analysis of regions of transgranular cracking revealed portions of the crack whose traces were near both slip and cleavage traces. Crack traces were observed to be nearer to slip traces than cleavage plane traces in a region of transgranular cracking, indicating hydrogen enhanced slip or dislocation movement may promote cracking on slip planes during HIC.

ACKNOWLEDGMENTS

The authors are grateful for the support of the sponsors of the Advanced Steel Processing and Products Research Center, an industry-university collaborative research center at the Colorado School of Mines.

REFERENCES

1. A. Brown and C.L. Jones, "Hydrogen-Induced Cracking in Pipeline Steels," *Corrosion*, Vol. 40, No. 7, 1984, pp. 330–336.
2. G. Domizzi, G. Anteri and J. Ovejero-García, "Influence of Sulphur Content and Inclusion Distribution on the Hydrogen-Induced Blister Cracking in Pressure Vessel and Pipeline Steels," *Corros. Sci.*, Vol. 43, No. 2, 2001, pp. 325–339.
3. F. Huang, J. Liu, Z.J. Deng, J.H. Cheng, Z.H. Lu and X.G. Li, "Effect of microstructure and inclusions on hydrogen-induced cracking susceptibility and hydrogen trapping efficiency of X120 pipeline steel," *Mater. Sci. Eng. A*, Vol. 527, No. 26, pp. 6997–7001, 2010.
4. J. Nieto, T. Elias, G. Lopez, G. Campos, F. Lopez, R. Garcia and A.K. De, "Development of technology for the production of HIC resistant slabs for sour service applications at ArcelorMittal Lazaro Cardenas , Mexico," *Materials Science and Technology Conference*, 2012, pp. 1044–1053.
5. NACE MR0175/ISO15156-2, "Petroleum and Natural Gas Industries — Materials for Use in H_2S Containing Environments in Oil and Gas Production — Part 2: Cracking-Resistant Carbon and Low Alloy Steel, and the Use of Cast Iron," 2003.
6. W.K. Kim, S.U. Koh, B.Y. Yang and K.Y. Kim, "Effect of Environmental and Metallurgical Factors on Hydrogen-Induced Cracking of HSLA Steels," *Corros. Sci.*, Vol. 50, No. 12, 2008, pp. 3336–3342.
7. X.B. Shi, W. Yan, W. Wang, L.Y. Zhao, Y.Y. Shan and K. Yang, "HIC and SSC Behavior of High-Strength Pipeline Steels," *Acta Metall. Sin. (English Lett.)*, Vol. 28, No. 7, 2015, pp. 799–808.
8. G.T. Park, S.U. Koh, H.G. Jung and K.Y. Kim, "Effect of Microstructure on the Hydrogen Trapping Efficiency and Hydrogen-Induced Cracking of Line Pipe Steel," *Corros. Sci.*, Vol. 50, No. 7, 2008, pp. 1865–1871.
9. S.U. Koh, H.G. Jung, K.B. Kang, G.T. Park and K.Y. Kim, "Effect of Microstructure on Hydrogen-Induced Cracking of Line Pipe Steels," *Corrosion*, Vol. 64, No. 7, 2008, pp. 574–585.
10. V. Venegas, F. Caleyo, J.M. Hallen, T. Baudin and R. Penelle, "Role of Crystallographic Texture in Hydrogen-Induced Cracking of Low-Carbon Steels for Sour Service Piping," *Metall. Mater. Trans. A.*, Vol. 38, No. 5, 2007, pp. 1022–1031.
11. V. Venegas, F. Caleyo, T. Baudin, J.M. Hallen and R. Penelle, "Role of Microtexture in the Interaction and Coalescence of Hydrogen-Induced Cracks," *Corros. Sci.*, Vol. 51, No. 5, 2009, pp. 1140–1145.
12. V. Venegas, F. Caleyo, J.L. González, T. Baudin, J.M. Hallen and R. Penelle, "Use of EBSD to Study Hydrogen-Induced Cracking in Pipeline Steel," *11th Int. Conf. Fract. 2005, ICF11*, Vol. 5, 2005, pp. 3430–3435.
13. V. Venegas, F. Caleyo, J.L. González, T. Baudin, J.M. Hallen and R. Penelle, "EBSD Study of Hydrogen-Induced Cracking in API-5L-X46 Pipeline Steel," *Scr. Mater.*, Vol. 52, No. 2, 2005, pp. 147–152.
14. M.A. Mohtadi-Bonab, M. Eskandari, K.M.M. Rahman, R. Ouellet and J.A. Szpunar, "An Extensive Study of Hydrogen-Induced Cracking Susceptibility in an API X60 Sour Service Pipeline Steel," *Int. J. Hydrogen Energy*, Vol. 41, No. 7, 2016, pp. 4185–4197.
15. M.A. Mohtadi-Bonab, J.A. Szpunar and S.S. Razavi-Tousi, "Hydrogen-Induced Cracking Susceptibility in Different Layers of a Hot-Rolled X70 Pipeline Steel," *Int. J. Hydrogen Energy*, Vol. 38, No. 31, 2013, pp. 13831–13841.
16. H.M. Al-Jabr, "Influence of Crystallographic Texture in X70 Pipeline Steels on Toughness Anisotropy and Delamination," Ph.D. dissertation, Colorado School of Mines, Golden, Colo., 2016.
17. V. Venegas, F. Caleyo, T. Baudin, J.H. Espina-Hernández and J.M. Hallen, "On the Role of Crystallographic Texture in Mitigating Hydrogen-Induced Cracking in Pipeline Steels," *Corros. Sci.*, Vol. 53, No. 12, 2011, pp. 4204–4212.
18. NACE Standard TM0284-2003, "Evaluation of Pipeline and Pressure Vessel Steels for Resistance to Hydrogen-Induced Cracking," 2003.
19. G. Angus, "Hydrogen-Induced Damage in Pipeline Steels," M.S. thesis, Colorado School of Mines, Golden, Colo., 2014.
20. V. Randle, H. Davies and I. Cross, "Grain Boundary Misorientation Distributions," *Curr. Opin. Solid State Mater. Sci.*, Vol. 5, No. 1, 2001, pp. 3–8.
21. V. Randle, "The Role of the Grain Boundary Plane in Cubic Polycrystals," *Acta Mater.*, Vol. 46, No. 5, 1997, pp. 1459–1480.
22. D.M. Saylor, B.S. El-Dasher, B.L. Adams and G.S. Rohrer, "Measuring the Five-Parameter Grain-Boundary Distribution From Observations of Planar Sections," *Metall. Mater. Trans. A*, Vol. 35, No. 7, 2004, pp. 1981–1989.

23. D.M. Saylor, B.S. El Dasher, A.D. Rollett and G.S. Rohrer, “Distribution of Grain Boundaries in Aluminum as a Function of Five Macroscopic Parameters ,” *Acta Mater.*, Vol. 52, No. 12, 2004, pp. 3649–3655.
24. F. Zhang and D.P. Field, “Characterization of Creep-Damaged Grain Boundaries of Alloy 617,” *Metall. Mater. Trans. A.*, Vol. 44, No. 11, 2013, pp. 4927–4936.
25. Z. Leng and D.P. Field, “Damage Susceptibility of Grain Boundaries in HT9 Steel Subjected to High-Temperature Creep,” *Metall. Mater. Trans. A.*, Vol. 43, No. 10, 2012, pp. 3539–3546.
26. V. Randle and A. Day, “Use of Rodrigues-Frank Space for Representation of Microtexture and Grain Boundary Parameters,” *Mater. Sci. Technol.*, Vol. 9, 1993, pp. 1069–1078.
27. H.K. Birnbaum and P. Sofronis, “Hydrogen-Enhanced Localized Plasticity — A Mechanism for Hydrogen-Related Fracture,” *Mater. Sci. Eng. A*, Vol. 176, No. 1–2, 1994, pp. 191–202.

